Geomagnetically induced currents during intense storms driven by coronal mass ejections and corotating interacting regions

Ryuho Kataoka[1,2] and Antti Pulkkinen[3,4]

Received 23 April 2007; revised 12 June 2007; accepted 10 July 2007; published 19 January 2008.

[1] Geomagnetically induced currents (GIC) flowing in ground-based conductor systems during large geomagnetic storms are one of the most significant space weather phenomena that affect our ground-based technological systems. Here we show that GIC activity in subauroral latitudes depends on the storm phase and on the interplanetary drivers, such as coronal mass ejections (CMEs) and corotating interacting regions (CIRs). For example, it is shown that GIC amplitudes are relatively small during CIR storms in comparison to CME storms. However, Pc3-5 pulsation activity during CIR storms drives long-lasting GIC in the local prenoon sector. Despite of the differences between CME and CIR storms, the relationship between GIC and the time derivative of the horizontal ground magnetic field is always the same. A novel power law equation is derived to accurately characterize the relation.

Citation: Kataoka, R., and A. Pulkkinen (2008), Geomagnetically induced currents during intense storms driven by coronal mass ejections and corotating interacting regions, *J. Geophys. Res.*, *113*, A03S12, doi:10.1029/2007JA012487.

1. Introduction

[2] Geomagnetically induced currents (GICs) flowing in long technological conductor networks on the ground are one of the manifestations of geomagnetic storms and can be thought as an end link of the chain of space weather processes from the surface of the Sun to the surface of the Earth. GIC poses a potential threat to the normal operation of technological systems such as power lines, pipelines, and railway systems [e.g., *Lanzerotti*, 1979; *Boteler et al.*, 1998].

[3] The fundamental challenge of GIC research is to identify, understand, and model the different geophysical processes associated with large GIC events. The present understanding is that a number of different geophysical processes are capable of driving large GICs; storm sudden commencements (SSC), geomagnetic pulsations, and auroral substorms have been identified as important causes for large GICs [*Boteler*, 2001; *Lam et al.*, 2002; *Kappenman*, 2003; *Pulkkinen et al.*, 2003, 2005].

[4] Most of the earlier studies, like those cited above, on the ionospheric and magnetospheric drivers of GICs have been more or less event based and did not provide any direct means for generalizations. Rigorous statistical analysis of GIC and the time derivative of the horizontal ground magnetic field (denoted hereafter dB/dt), a quantity closely coupled to GIC via Faraday's law of induction, have been carried out by *Viljanen* [1997], *Viljanen et al.* [2001, 2006], *Weigel et al.* [2002], *Weigel and Baker* [2003], *Wintoft* [2005], and *Pulkkinen et al.* [2006].

[5] However, basic characteristics of GIC during intense storms are still not well known. Recently, *Pulkkinen and Kataoka* [2006] performed a time-frequency analysis of GICs during the 10 greatest superstorms to show a clear local time and storm phase dependence of the GIC spectra. Such superstorms are driven by fast coronal mass ejections (CMEs) [e.g., *Kataoka et al.*, 2005]. *Miyoshi and Kataoka* [2005] showed evidence that there are significant differences in the magnetospheric response between intense storms driven by CMEs and corotating interaction regions (CIRs), and therefore the GIC response is also expected to be different for the CME and CIR storms. The purpose of this study is to investigate the possible differences of GIC variations between CME and CIR storms.

2. Data and the Analysis Method

[6] The main data to be analyzed is composed of GIC measurements carried out since November 1998 in the Finnish natural gas pipeline at the Mäntsälä pipeline section [*Pulkkinen et al.*, 2001]. The magnetic latitude of the measurement site is about 57 degrees, and the magnetic local time is about UT plus 3 h. The GIC data are obtained with a 10 s temporal resolution. The IMAGE magnetometer chain [*Lühr et al.*, 1998] is used to provide more general geomagnetic context. Nurmijärvi Geophysical Observatory (NUR), a part of the IMAGE chain, is located about 30 km southwest from the GIC measurement site. Also, the magnetometer data are obtained with a 10 s temporal resolution. Table 1 lists the coordinates of the IMAGE magnetometer stations used in this study.

[7] Figure 1 shows a correlation between minimum *Dst* and maximum GIC for the isolated intense storms (mini-

[1]Computational Astrophysics Laboratory, Institute of Physics and Chemical Research (RIKEN), Saitama, Japan.
[2]Solar-Terrestrial Laboratory, Nagoya University, Nagoya, Japan.
[3]Goddard Earth Sciences and Technology Center, University of Maryland, Baltimore County, Baltimore, Maryland, USA.
[4]NASA Goddard Space Flight Center, Greenbelt, Maryland, USA.

0148-0227/08/2007JA012487

Table 1. Coordinates of IMAGE Magnetometer Stations Used in This Study

Abbreviation	Name	GEO Latitude	GEO Longitude	CGM Latitude	CGM Longitude
NAL	Ny Ålesund	78.92	11.95	75.25	112.08
LYR	Longyearbyen	78.20	15.82	75.12	113.00
HOR	Hornsund	77.00	15.60	74.13	109.59
SOR	Sørøya	70.54	22.22	67.34	106.17
KIL	Kilpisjärvi	69.02	20.79	65.88	103.79
MUO	Muonio	68.02	23.53	64.72	105.22
PEL	Pello	66.90	24.08	63.55	104.92
OUJ	Oulujärvi	64.52	27.23	60.99	106.14
HAN	Hankasalmi	62.30	26.65	58.71	104.61
NUR	Nurmijärvi	60.50	24.65	56.89	102.18
TAR	Tartu	58.26	26.46	54.47	102.89

mum $Dst < -100$ nT) during solar cycle 23 (years 1996 to 2005) as identified by *Kataoka and Miyoshi* [2006]. Continuous GIC data are available for 32 CME storms and 3 CIR storms, as indicated by open and solid circles, respectively. The superstorms investigated by *Pulkkinen and Kataoka* [2006] are included in the CME storms only if the superstorms are isolated without multiple occurrences of intense storms within 4 d. The maximum amplitude of GIC is calculated for the time interval 1 d before and after the *Dst* minima. The correlation coefficient is 0.67 for CME storms, implying that large GIC events tend to be associated with large CME storms.

[8] As is seen from Figure 1, the three CIR storms are smaller in amplitude both in terms of *Dst* and GIC. The small number of CIR storms is due to the fact that CIRs rarely produce intense storms. In fact, typical CIRs have a limited interplanetary magnetic field strength of up to about 20 nT [*Richardson et al.*, 2006]. However, since intense CIR storms can be a potential cause for large GIC events, it is worthwhile to include these events in our analysis.

[9] Generally, the waveform of GICs tends to be very noisy and nonstationary [*Pulkkinen and Kataoka*, 2006]. The S-transform [*Stockwell et al.*, 1996], capable of handing the noisy nonstationary data, is a time-frequency analysis of a time series h(t) and is defined as:

$$S(\tau, f) = \int_{-\infty}^{\infty} h(t) \frac{|f|}{\sqrt{2\pi}} e^{\frac{-f^2(\tau-t)^2}{2}} e^{-i2\pi ft} dt, \qquad (1)$$

where τ is time and f is frequency. The kernel of the S-transform is defined by a Gaussian with the window width of 1/f to give the best resolution in time-frequency space. The normalized Gaussian kernel also gives a direct mathematical connection to the Fourier transform via the integration over τ.

[10] Before calculating the S-transform spectra of GIC for all 24-h long segments centered around *Dst* minima of storm events, there are three preprocessing steps as follows: (1) We include the margins of 2 h time series just before and after the 24-h time series to reduce an artificial edge effects; (2) Hanning window is applied on the 5% of the total 28 $\times$ 360 points at the edges to further reduce the edge effect; (3) Hilbert transform is applied to obtain the analytic signal in which the spectral power is localized into positive frequencies. Finally, we apply the S-transform to the analytic signal, and the amplitude $|S(\tau, f)|$ is color coded to display the S-transform spectra.

3. Results

[11] First, we show typical examples of the GIC spectra during comparable nightside CME and CIR storm events. The *Dst* minima for the selected CME and CIR storms are -110 nT at 1930 UT (2230 MLT) on 11 May 2002 and -109 nT at 1730 UT (2030 MLT) on 11 February 2004, respectively. Using the nightside events, we can directly compare the results with the results for superstorms, as shown by *Pulkkinen and Kataoka* [2006].

[12] Figures 2 and 3 show GIC and the S-transform of GIC for the selected events. It is seen that around the storm peak taking place in the nightside, turbulent broadband spectra are seen in both CME and CIR storms. After the storm peak, the CIR storm has a stronger and longer-lasting GIC activity than that of the CME storm even though the *Dst* minima for the storms are similar to each other. Local daytime GIC in Pc3-5 pulsation ranges (0.3–10 min) are

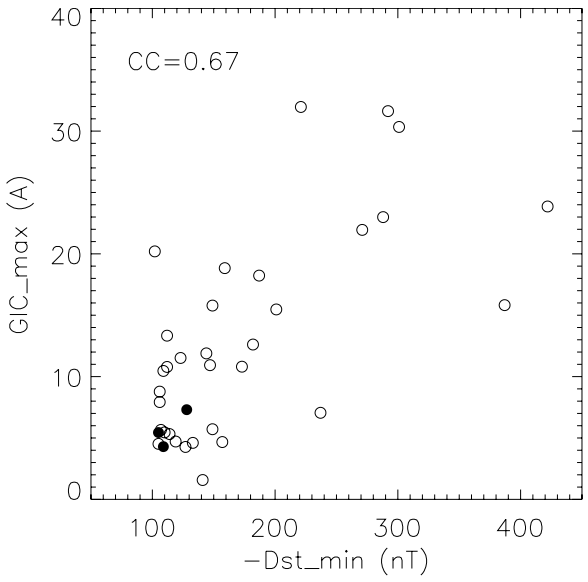

Figure 1. Scatterplot of maximum |*Dst*| and |GIC| for each of the $Dst < -100$ nT storms used in this study. Coronal mass ejection (CME) storms are indicated by open circles and corotating interaction regions (CIR) storms by solid circles.

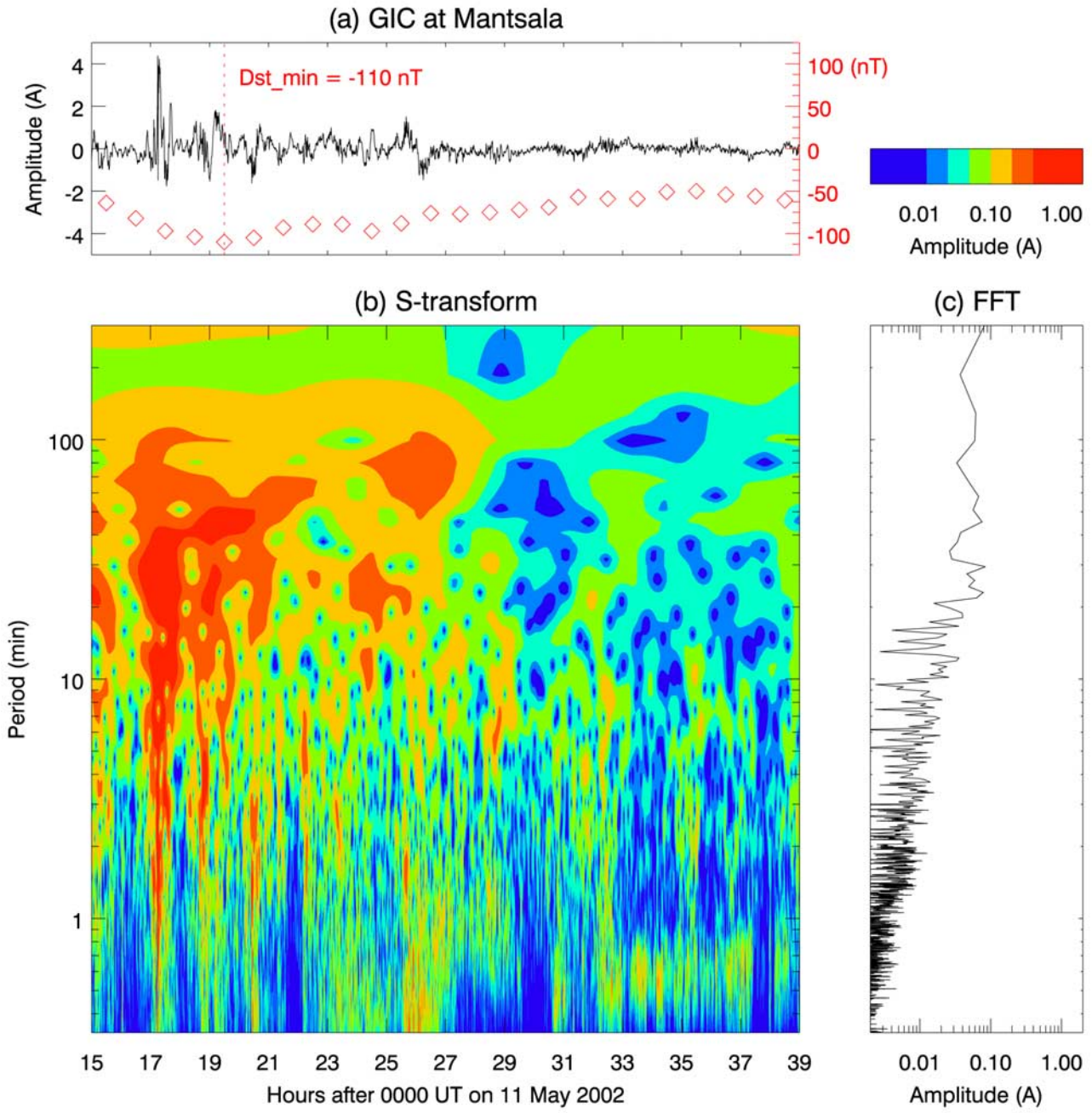

Figure 2. S-transform spectrum of a CME storm on 11 May 2002 showing (a) the waveform of geomagnetically induced currents (GIC), (b) the S-transform spectral power, and (c) the FFT power spectrum obtained by integrating the S-transform over time. The left half of Figure 2b is the local nightside (1800–0600 MLT), and the right half is the local dayside (0600–1800 MLT). Red diamonds indicate the *Dst* index. The storm peak is shown by a vertical dotted line.

especially enhanced during the recovery phase of the CIR storm. Comparing the Figures 2c and 3c, the GIC enhancement in the Pc3-5 range during the CIR storm can also be seen from the FFT spectra. Strong monochromatic GIC in the Pc5 range (2.5–10 min), as was seen for superstorms by *Pulkkinen and Kataoka* [2006], is not present during the recovery phase of the CME storm. Although not shown here, the spectral features observed above are common also for the other CME and CIR storms studied in this work.

[13] We then compare the time derivative of the horizontal magnetic field (dB/dt) observed at NUR with the GIC using all of the CME and CIR storm events. The time derivative is calculated by using the three-point central difference formula. To compare the GIC and dB/dt, the data are divided into 1 h intervals, each containing 360 sample points. The maximum amplitudes of |dB/dt| and |GIC| are calculated in each interval, and 1 h values are obtained for four different time intervals: just after the storm

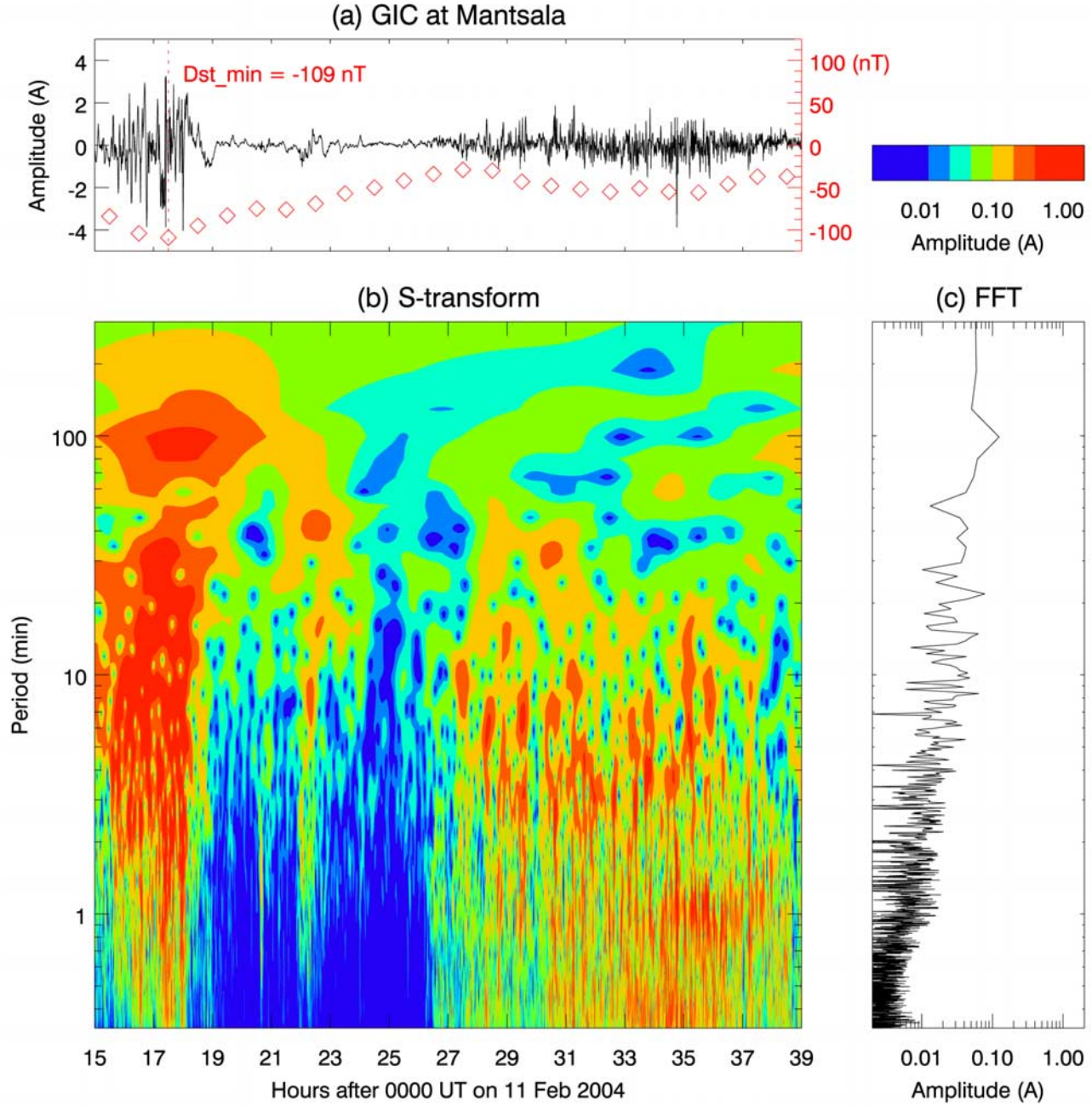

Figure 3. S-transform spectrum of a CIR storm on 11 February 2004. The format is the same as in Figure 2.

sudden commencement (SSC), main phase, recovery phase, and 24 h after the end of the recovery phase.

[14] In this paper, the beginning of the main phase is determined by the existence of minimum d(*Dst*)/dt or two successive points of d(*Dst*)/dt < −20 nT/h, where the time derivative is calculated using a two-point forward difference formula. If it is not possible to detect the beginning by these criteria, a typical time period of 6 h before the *Dst* minimum is taken as the main phase interval. The end of the recovery phase is determined by the recovery of the *Dst* index to 50% of the *Dst* minimum. If it is not possible to detect the end by these criteria, typical time period of 12 h after the *Dst* minimum is taken as the recovery phase interval.

[15] From Figure 4 showing the scatterplot and histograms of maximum |dB/dt| and |GIC| for CME storms, it is seen that from the main phase (red) to the recovery phase (blue) the amplitudes of |GIC| and |dB/dt| decrease more than a half an order of magnitude on average. Further, from the recovery phase (blue) to the 24 h after the end of the recovery phase (green), the amplitudes decrease again more than a half an order of magnitude on average. However, independent of the storm phase, all of the data points distribute around the same regression line. The correlation coefficient is better for |dBy/dt| (CC = 0.97) than that of |dBx/dt| (CC = 0.94), where the subscripts x and y denote the geographic north-south and east-west components, re-

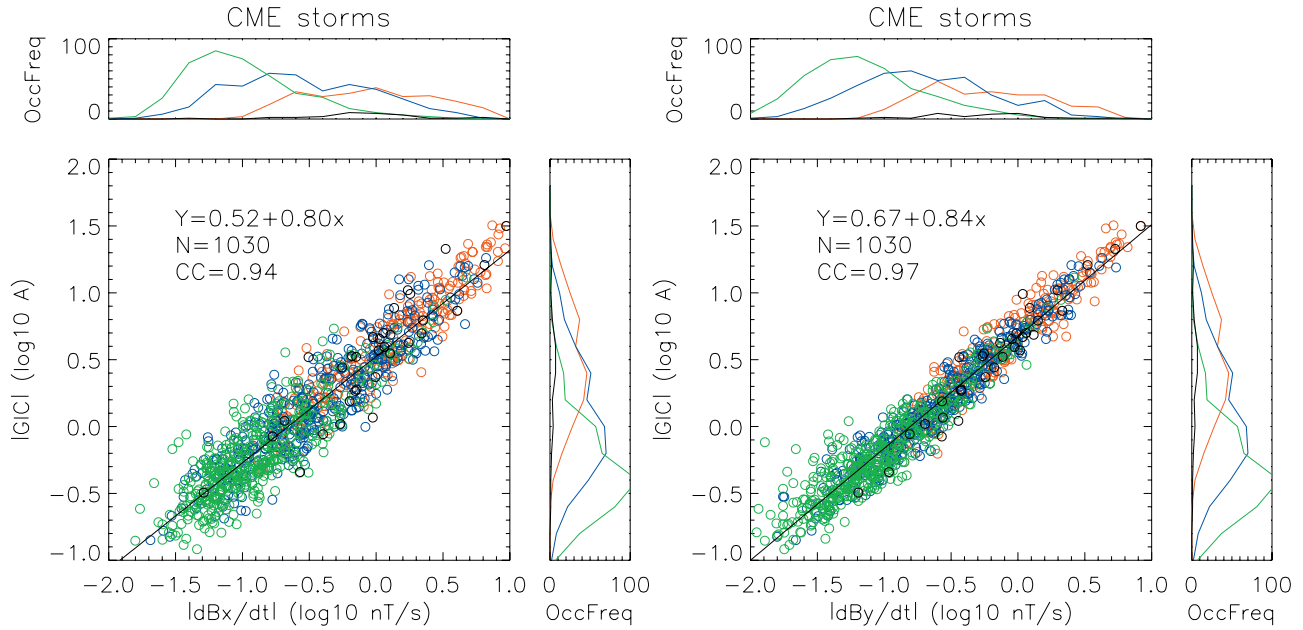

Figure 4. Scatterplot and histograms of maximum |dB/dt| showing (left) the x-component and (right) y-component and maximum |GIC| during the main phase (red), recovery phase (blue), 24 h after the end of recovery phase (green), and just after the storm sudden commencements (black) of CME storms.

spectively. The difference in correlation clearly reflects the geographical orientation of the pipeline; GIC flow in the pipeline responds differently for east-west and north-south geoelectric field in association with the temporal changes of the magnetic field [*Pulkkinen et al.*, 2001]. The relationship between |dBy/dt| and |GIC| can be approximated by power-law equation,

$$|\mathrm{GIC}|(\mathrm{A}) = 10^{0.67}|dB_y/dt|^{0.84}(\mathrm{nT/s}). \quad (2)$$

From Figure 5 showing the scatter plot and histograms of maximum |dB/dt| and |GIC| for CIR storms, it is seen that although the correlation between the two quantities is slightly worse, the basic trend of the regression line is the same as that for the CME storms. Again, the correlation coefficient is better for |dBy/dt| (CC = 0.91) than that of |dBx/dt| (CC = 0.78). The approximately log-normal histograms in Figures 4 and 5 suggest that the GIC amplitude rarely exceeds the 10 A level even in the main phase of CIR storms. From Figure 5 it is also seen that the storm phase dependence of the |dB/dt| and |GIC| amplitudes

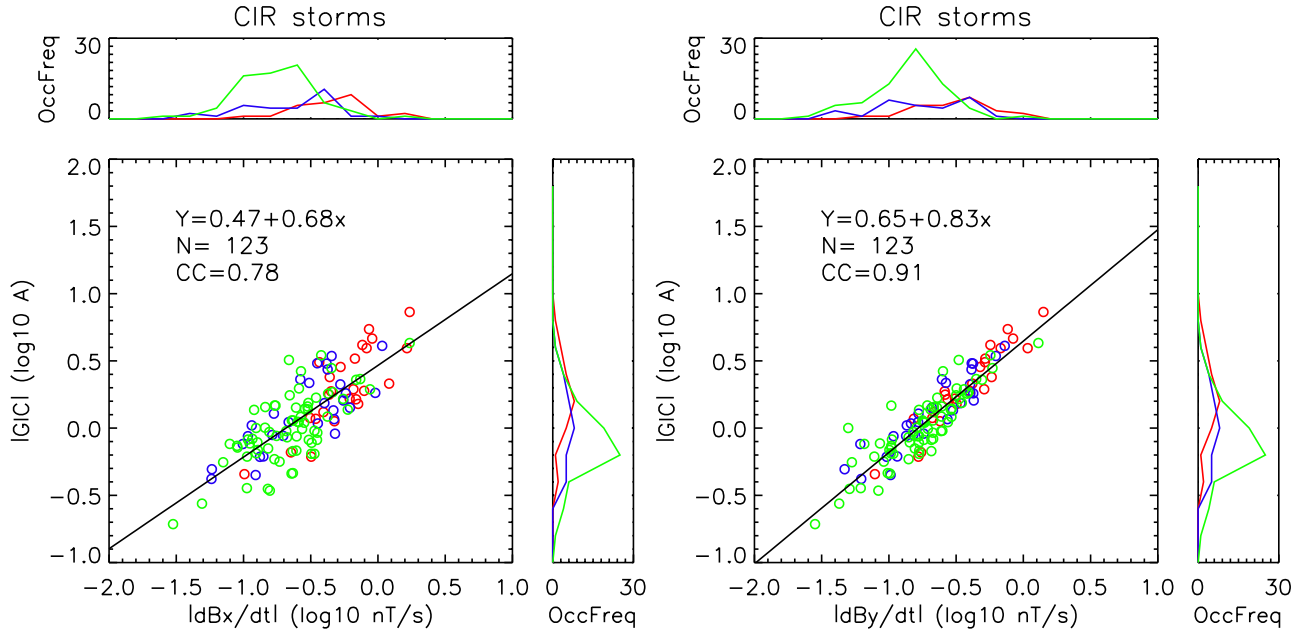

Figure 5. Same as Figure 4 but for CIR storms.

Table 2. Statistical Parameters of |GIC| Amplitudes for Different Storm Phases[a]

Interplanetary Driver	Storm Phase	Total Number of Storms	Total Number of Hours	Average (A)	Maximum (A)
CME	SSC	32	32	3.3	31.6
CME	main	32	247	3.8	32.0
CME	recovery	32	380	1.5	18.2
CME	after recovery	32	403	0.6	13.0
CIR	main	3	25	2.0	7.3
CIR	recovery	3	29	1.3	4.1
CIR	after recovery	3	69	1.0	4.3

[a]From left to right, columns show the storm driver, storm phase, the total number of the storm events, the total number of sample hours, mean values, and maximum values.

is relatively small for CIR storms, ranging well below an order of magnitude on average. Comparing the recovery phase (blue) and late recovery phase (green) in Figures 4 and 5, it is apparent, in agreement with Figures 2 and 3, that the |dB/dt| and |GIC| amplitudes during the recovery and late recovery phases are larger for CIR storms on average. Some statistical parameters of |GIC| are summarized in Table 2. The mean values are calculated after taking the logarithm. This is reasonable since the hourly values of both |GIC| and |dB/dt| follow the log-normal distribution as show in the histograms in Figures 4 and 5.

4. Discussion

[16] Figures 2 and 3 imply that partially different physical mechanisms drive GIC during CME and CIR storms. The most interesting observation is that, during CIR storms, GIC is enhanced in the Pc3-5 pulsation range, especially in the local dayside during the recovery phase. The Pc3-5 pulsations are related to the high-speed Alfvénic solar wind streams originating from large coronal holes [see *Richardson et al.*, 2006]. Thus these coronal hole streams are the origin for the long-lasting GIC activity during CIR storms. On the other hand, for the February 2004 event shown in Figure 3, the very quiet period of GIC lasting 8 h just after the storm peak was associated with unusually stable northward interplanetary magnetic fields embedded within the CIR and is not necessarily a general feature of CIR-associated storms.

[17] The well-known correlation of Pc3-5 pulsation wave power with the solar wind speed [*Singer et al.*, 1977; *Engebretson et al.*, 1998], suggests that the Kelvin-Helmholtz instabilities (KHI) at the magnetopause may act as a possible energy source for the pulsations. Actually, using multiple in situ satellite observations, *Rae et al.* [2005] investigated very strong narrowband monochromatic Pc5 pulsation, as seen in GIC during superstorms [*Pulkkinen and Kataoka*, 2006] and concluded that the discrete Pc5 pulsation is the result from the excitation of a magnetospheric waveguide mode driven by KHI at the magnetopause. Other mechanisms, however, possibly contribute to large GIC in the Pc3-5 range. On the basis of the IMAGE magnetometer data, *Howard and Menk* [2005] suggested that the daytime Pc3-4 waves as observed in this paper are generated by the upstream ion-cycrotron resonance and that there is no evidence of generation by the KHI. *Baker et al.* [2003] surveyed a 10-year data set of CANOPUS to statistically investigate the Pc5 pulsation and suggested from the property of field-line resonance that the energy source of Pc5 pulsation is not only KHI but also that a significant part of the Pc5 pulsations should have some irregular or impulsive energy source such as traveling indentations on the magnetopause [*Mathie and Mann*, 2000] or solar wind buffeting. They also noted that transient events such as magnetic impulse events [e.g., *Kataoka et al.*, 2001] contribute to the largest power of Pc5 spectra in a limited dawn sector between 65 to 70 magnetic latitudes.

[18] Despite the spectral differences found between CME and CIR storms, hourly dB/dt is found always to be an excellent indicator of the hourly GIC activity, and the relationship between the GIC and the dB/dt is always the same in a very large dynamic range of about three orders of magnitude, as shown in Figures 4 and 5. This finding is in agreement with earlier results [see, e.g., *Viljanen et al.*, 2001, and references therein]; the novel result is that the relationship can be made very accurate by using the functional form given in equation (2). It should be noted here that there are examples [*Trichtchenko and Boteler*, 2006] where GIC behavior follows the magnetic field strength (B) rather than its time derivative**.** However, by making plots similar to Figures 4 and 5 for B, we have confirmed that dB/dt is a better indicator for GIC activity than B at Mäntsälä.

[19] For additional insights to |dB/dt| behavior, as shown in Figure 6, we construct a polar map showing the global distribution of average amplitude of the hourly maximum |dB/dt| and root mean square of the hourly maximum |dBx/dt| and |dBy/dt|. We use the eleven meridional magnetometers listed in Table 1. All six CIR events in the list of *Kataoka and Miyoshi* [2006] and an additional recent CIR event that occurred in the end of August 2005 are used in constructing the map. However, even with the additional CIR events the number of data points was, unfortunately, too small to construct a map for the CIR main phase. A total of 11 $\times$ 24 average points (11 points in latitude and 24 points in MLT) are linearly interpolated and color contoured. Note again that the average values are calculated after taking the logarithm.

[20] *Weigel et al.* [2002, 2003] computed similar average polar maps of |dB/dt|, but they did not make a classification of different storm phases. The results here indicate that it may be beneficial to separate predictions of |dB/dt| by different classes based on, for example, storm phase and interplanetary driver. For example, the prenoon peak of CIR storms (Figure 6c) is about twice as strong on average than that of CME storms (Figure 6b). Further, comparing the Figures 6a and 6b, the local time sector having the greatest activity may vary as a function of CME storm phase, for

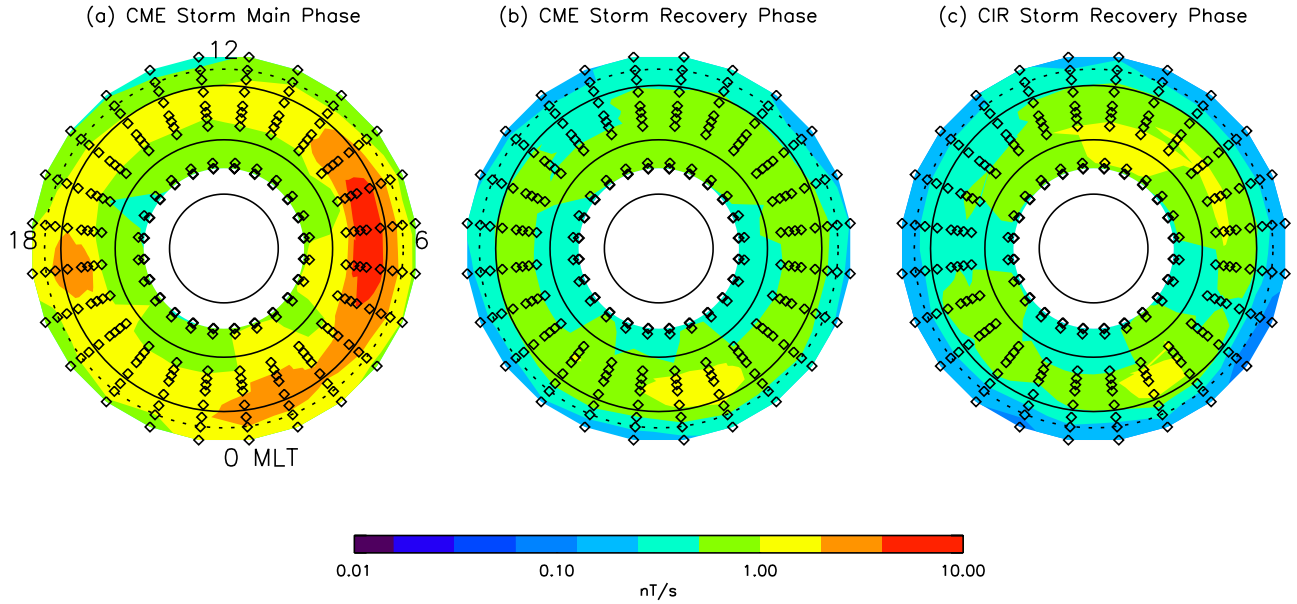

Figure 6. Polar map of the average amplitude of the hourly maximum |dB/dt| during (a) the main phase and (b) the recovery phase of CME storms and (c) during and 24 h after the recovery phase of CIR storms. Solid lines indicate the 80, 70, and 60 MLAT, and the dotted line indicates the latitude of the NUR station. Open squares indicate the meridional locations of the IMAGE chain.

example, the greatest activity is appeared in the dawn and postmidnight sector during the main and recovery phase, respectively.

5. Conclusions

[21] It was shown that subauroral GIC activity depends on the solar wind driver and phases of strong geomagnetic storms. For example, GIC amplitudes are relatively small during CIR storms in comparison to CME storms. However, Pc3-5 pulsation activity during CIR storms drives long-lasting GIC in the local prenoon sector. Despite of the differences, the maximum hourly value of |dB/dt| is always an excellent indicator for the maximum hourly amplitude of |GIC| in the Finnish pipeline for any local time and any storm phase of CME/CIR storms. A novel power law equation was derived to accurately characterize the relationship between |dB/dt| and |GIC|.

[22] **Acknowledgments.** GIC measurements in the Finnish pipeline owned by the Gasum Oy Company are carried out by the Finnish Meteorological Institute. A. Viljanen of Finnish Meteorological Institute is acknowledged for providing the GIC data used in the study. We thank the institutes who maintain the IMAGE magnetometer array. The work by RK was supported by a research fellowship of the Japan Society for the Promotion of Science for Young Scientists and a research fellowship of Special Postdoctoral Research Program at RIKEN. This work was supported by the Grant-in-Aid for Creative Scientific Research "The Basic Study of Space Weather Prediction" (17GS0208, Head Investigator: K. Shibata) from the Ministry of Education, Science, Sports, Technology, and Culture of Japan.

[23] Amitava Bhattacharjee thanks Ian Richardson and Yusuke Ebihara for their assistance in evaluating this paper.

References

Baker, G. J., E. F. Donovan, and B. J. Jackel (2003), A comprehensive survey of auroral latitude Pc5 pulsation characteristics, *J. Geophys. Res.*, *108*(A10), 1384, doi:10.1029/2002JA009801.

Boteler, D. (2001), Assessment of geomagnetic hazards to power systems in Canada, *Natural Hazards*, *23*, 101–120.

Boteler, D. H., R. J. Pirjola, and H. Nevanlinna (1998), The effects of geomagnetic disturbances on electrical systems at the Earth's surface, *Adv. Space Res.*, *22*, 17–27.

Engebretson, M., K.-H. Glassmeier, M. Stellmacher, W. J. Hughes, and H. Luhr (1998), The dependence of a high latitude Pc5 wave power on solar wind velocity and on the phase of high speed solar wind streams, *J. Geophys. Res.*, *103*, 26,271.

Howard, T. A., and F. W. Menk (2005), Ground observations of high-latitude Pc3-4 ULF waves, *J. Geophys. Res.*, *110*, A04205, doi:10.1029/2004JA010417.

Kappenman, J. G. (2003), Storm sudden commencement events and the associated geomagnetically induced current risks to ground-based systems at low-latitude and midlatitude locations, *Space Weather*, *1*(3), 1016, doi:10.1029/2003SW000009.

Kataoka, R., and Y. Miyoshi (2006), Flux enhancement of radiation belt electrons during geomagnetic storms driven by coronal mass ejections and corotating interaction regions, *Space Weather*, *4*, S09004, doi:10.1029/2005SW000211.

Kataoka, R., H. Fukunishi, L. J. Lanzerotti, C. G. Maclennan, H. U. Frey, S. B. Mende, J. H. Doolittle, T. J. Rosenberg, and A. T. Weatherwax (2001), Magnetic Impulse Event: A detailed case study of extended ground and space observations, *J. Geophys. Res.*, *106*, 25,873–25,889.

Kataoka, R., S. Watari, N. Shimada, H. Shimazu, and K. Marubashi (2005), Downstream structures of interplanetary fast shocks associated with coronal mass ejections, *Geophys. Res. Lett.*, *32*, L12103, doi:10.1029/2005GL022777.

Lam, H.-L., D. H. Boteler, and L. Trichtchenko (2002), Case studies of space weather events from their launching on the Sun to their impacts on power systems on the Earth, *Ann. Geophys.*, *20*, 1073–1079.

Lanzerotti, L. J. (1979), Geomagnetic influences on man-made systems, *J. Atmos. Terr. Phys.*, *41*, 787–796.

Lühr, H., A. Aylward, S. C. Bucher, A. Pajunpaa, K. Pajunpaa, T. Holmboe, and S. M. Zalewski (1998), Westward moving dynamic substorm features observed with the IMAGE magnetometer network and other ground-based instruments, *Ann. Geophys.*, *16*, 425–440.

Mathie, R. A., and I. R. Mann (2000), Observations of Pc5 field line resonance azimuthal phase speeds: A diagnostic of their excitation mechanism, *J. Geophys. Res.*, *105*, 10,713–10,728.

Miyoshi, Y., and R. Kataoka (2005), Ring current ions and radiation belt electrons during geomagnetic storms driven by coronal mass ejections and corotating interaction regions, *Geophys. Res. Lett.*, *32*, L21105, doi:10.1029/2005GL024590.

Pulkkinen, A., and R. Kataoka (2006), S-transform view of geomagnetically induced currents during geomagnetic superstorms, *Geophys. Res. Lett.*, *33*, L12108, doi:10.1029/2006GL025822.

Pulkkinen, A., A. Viljanen, K. Pajunpää, and R. Pirjola (2001), Recordings and occurrence of geomagnetically induced currents in the Finnish natural gas pipeline network, *J. Appl. Geophys.*, *48*, 219–231.

Pulkkinen, A., A. Thomson, E. Clarke, and A. McKay (2003), April 2000 storm: ionospheric drivers of large geomagnetically induced currents, *Ann. Geophys.*, *21*, 709–717.

Pulkkinen, A., S. Lindahl, A. Viljanen, and R. Pirjola (2005), Geomagnetic storm of 29–31 October 2003: Geomagnetically induced currents and their relation to problems in the Swedish high-voltage power transmission system, *Space Weather*, *3*, S08C03, doi:10.1029/2004SW000123.

Pulkkinen, A., A. Viljanen, and R. Pirjola (2006), Estimation of geomagnetically induced current levels from different input data, *Space Weather*, *4*, S08005, doi:10.1029/2006SW000229.

Rae, I. J., et al. (2005), Evolution and characteristics of global Pc5 ULF waves during a high solar wind speed interval, *J. Geophys. Res.*, *110*, A12211, doi:10.1029/2005JA011007.

Richardson, I. G., et al. (2006), Major geomagnetic storms (Dst < −100 nT) generated by corotating interaction regions, *J. Geophys. Res.*, *111*, A07S09, doi:10.1029/2005JA011476.

Singer, H. J., C. T. Russel, M. G. Kivelson, E. Q. Greenstadt, and J. V. Olson (1977), Evidence for the control of Pc3-4 magnetic pulsations by the solar wind velocity, *Geophys. Res. Lett.*, *4*, 377–381.

Stockwell, R. G., L. Manshinha, and R. P. Lowe (1996), Localization of the complex spectrum: The S-transform, *IEEE Trans. Signal Proc.*, *44*(4), 998–1001.

Trichtchenko, L., and D. Boteler (2006), Response of power systems to the temporal characteristics of geomagnetic storms, paper presented at Canadian Conference on Electrical and Computer Engineering, IEEE, Ottawa, Ontario, Canada.

Viljanen, A. (1997), The relation between geomagnetic variations and their time derivatives and implications for estimation of induction risks, *Geophys. Res. Lett.*, *24*, 631–634.

Viljanen, A., H. Nevanlinna, K. Pajunpää, and A. Pulkkinen (2001), Time derivative of the horizontal magnetic field as an activity indicator, *Ann. Geophys.*, *19*, 1107–1118.

Viljanen, A., E. I. Taskanen, and A. Pulkkinen (2006), Relation between substorm characteristics and rapid temporal variations of the ground magnetic field, *Ann. Geophys.*, *24*, 725–733.

Weigel, R. S., and D. N. Baker (2003), Probability distribution invariance of 1-minute auroral-zone geomagnetic field fluctuations, *Geophys. Res. Lett.*, *30*(23), 2193, doi:10.1029/2003GL018470.

Weigel, R. S., D. Vassiliadis, and A. J. Klimas (2002), Coupling of the solar wind to temporal fluctuations in ground magnetic fields, *Geophys. Res. Lett.*, *29*(19), 1915, doi:10.1029/2002GL014740.

Weigel, R. S., A. J. Klimas, and D. Vassiliadis (2003), Solar wind coupling to and predictability of ground magnetic fields and their time derivatives, *J. Geophys. Res.*, *108*(A7), 1298, doi:10.1029/2002JA009627.

Wintoft, P. (2005), Study of the solar wind coupling to the time difference horizontal geomagnetic field, *Ann. Geophys.*, *23*, 1949–1957.

R. Kataoka, Computational Astrophysics Laboratory, Institute of Physics and Chemical Research (RIKEN), 2-1 Hirosawa, Wako, Saitama 351-0198, Japan. (ryuho@riken.jp)

A. Pulkkinen, NASA Goddard Space Flight Center, Code 674, Greenbelt, MD 20771, USA. (antti.pulkkinen@gsfc.nasa.gov)